

# Effect of rhenium and ruthenium on the deformation and fracture mechanism in nickel-based model single crystal superalloys during the *in-situ* tensile at room temperature

C.P. Liu<sup>a</sup>, X.N. Zhang<sup>a,\*</sup>, L. Ge<sup>a</sup>, S.H. Liu<sup>b</sup>, C.Y. Wang<sup>c,d</sup>, T. Yu<sup>d</sup>, Y.F. Zhang<sup>a</sup>, Z. Zhang<sup>e,\*\*</sup>

<sup>a</sup> Institute of Microstructure and Property of Advanced Materials, Beijing University of Technology, Beijing 100124, China

<sup>b</sup> School of Materials Science and Engineering, Tsinghua University, Beijing 100084, China

<sup>c</sup> Department of Physics, Tsinghua University, Beijing 100084, China

<sup>d</sup> Central Iron and Steel Research Institute, Beijing 100081, China

<sup>e</sup> State Key Laboratory of Silicon Materials and Department of Materials Science and Engineering, Zhejiang University, Hangzhou 310027, China

## ARTICLE INFO

### Keywords:

Nickel-based model single crystal superalloys

*In-situ* tensile experiment

Fracture

Dislocation configurations

## ABSTRACT

*In-situ* tensile experiments of Ni-Al, Ni-Al-Re and Ni-Al-Re-Ru model single-crystal superalloys were performed in scanning electron microscope (SEM) at room temperature. The plastic deformation mechanisms of all the three model superalloys were double-oriented slipping of dislocations. Micro-cracks were often formed at the intersection of two sets of slip lines. The fracture surfaces of Ni-Al and Ni-Al-Re-Ru alloys were nearly parallel to (010) planes and that of the Ni-Al-Re alloys was nearly parallel to (1–11) plane. The dislocation configuration was analyzed by transmission electron microscopy (TEM). The  $a/2 < 110 >$  dislocation pairs coupled with antiphase boundary (APB) cut into  $\gamma'$  phase in the Ni-Al and Ni-Al-Re-Ru model superalloys. In addition to these dislocations, stacking faults also cut into  $\gamma'$  phase in Ni-Al-Re model superalloys. The different fracture surfaces of different model single-crystal superalloys were attributed to the influence of elements Re and Ru on the dislocation configuration.

## 1. Introduction

Nickel-based single crystal superalloys consist of cubical  $\gamma'$  phases with  $L1_2$  structure embedded coherently in  $\gamma$  matrix with a face-centered cubic structure. They have been widely used to manufacture advanced gas turbines because of their excellent creep and fatigue strength [1,2]. With the increasing demand of service performance, many different elements have been added into superalloys. As the second and the third generation symbolic element, rhenium (Re) has been found to reduce  $\gamma'$  coarsening and significantly improve the creep property at high temperature [3–5]. However, an excess of Re decreases the creep strength by separation of hard, brittle topologically close-packed (TCP) phases [6,7]. The formation of TCP phases could be inhibited by adding ruthenium (Ru) [8]. Superalloys incorporating Ru are considered to be the fourth-generation superalloys with improved microstructural stability and creep resistance [9,10]. It is therefore important to understand the effect of Re and Ru on the microstructure and the microstructural evolution in the service process of nickel-based single crystal superalloys.

Fracture of superalloys often results from micro-crack generation and propagation. Investigating the effect of elements Re and Ru on the fracture process and microstructural evolution will increase our understanding of the role of each element. Most studies to date have concentrated on the generation location and propagation process of the micro-cracks. Micro-cracks are usually generated at the interfaces between the TCP phase and the  $\gamma$  matrix or the region of stress concentration interaction [11–13]. There are different opinions about the way crack propagation. Ott et al. posited that the cracks propagated along the  $\gamma$  channels or the  $\gamma/\gamma'$ -interfaces after rafting [14]. Tian et al. reported that cracks firstly propagated on the {001} and then along {111} planes during 760 °C/800 MPa creep process [12]. Feng et al. concluded that the crack mainly propagated along the TCP / $\gamma'$  interface [15]. Moverare et al. believed that crack propagation rapidly occurred along twinning planes during thermal–mechanical fatigue testing [13]. However, few researchers reported the effect of the alloying elements on micro-cracks generation and propagation. Further research on the effect of Re and Ru on the deformation and fracture mechanism of the superalloys is necessary.

<sup>\*\*</sup> Corresponding author.

<sup>\*</sup> Corresponding author.

E-mail addresses: [xnzhang@bjut.edu.cn](mailto:xnzhang@bjut.edu.cn) (X.N. Zhang), [zezhang@zju.edu.cn](mailto:zezhang@zju.edu.cn) (Z. Zhang).

In this study, the plastic deformation and fracture behaviors of Ni-Al, Ni-Al-Re and Ni-Al-Re-Ru model single crystal superalloys were investigated by *in-situ* tensile experiments in SEM at room temperature. The dislocation configurations were analyzed using TEM. The purpose of these investigations was to understand the effect of Re and Ru on the plastic deformation and fracture mechanism of the superalloys.

## 2. Materials and experimental methods

Three types of Ni-based model single crystal superalloys were designed to study the effect of Re and Ru on the deformation and fracture mechanism. The chemical compositions (by wt%) of these alloys are listed in Table 1. The model superalloys were directionally solidified to form a [001] oriented single-crystal. A solution treatment was performed at 1330 °C for 20 h under flowing argon followed by water cooling, and an aging treatment was performed at 870 °C for 32 h followed by water cooling.

**Table 1**

Chemical compositions of three types model superalloys (wt%).

	Ni	Al	Re	Ru
Ni-Al	91.23	8.77	–	–
Ni-Al-Re	86.69	8.31	5.00	–
Ni-Al-Re-Ru	83.80	8.20	5.00	3.00

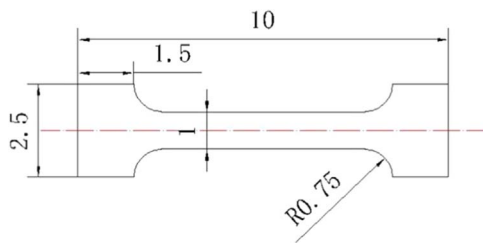


**Fig. 1.** The size of the tensile sample (mm).

The size of tensile sample was shown in Fig. 1. The samples for SEM were electrochemical etched using a solution of 40% nitric acid, 12% phosphoric acid and 48% vitriol (by volume fraction) at 5 V. The *in-situ* uniaxial tensile experiments were performed using a micro drawing mill, which was installed in SEM FEI Quanta250. The tensile axis was parallel to the [010] direction with a deviation angle less than 10 degrees. The experiments were performed at a constant strain rate of  $1.4 \times 10^{-4} \text{ s}^{-1}$ . At least three samples for each type of model superalloys were stretched to minimize experimental errors. The samples for TEM were selected to be around 2 mm away from the fracture surface. The slices cut from samples were mechanically ground and polished to a thickness of 40  $\mu\text{m}$ , and then the slices were thinned using a Gatan precision ion polisher system (PIPS) at 2–3 keV. TEM investigation was performed using JEM-2010F microscope operated at an accelerating voltage of 200 kV. The average size of  $\gamma'$  precipitates for three model superalloys was measured using the Adobe Photoshop and Image-Pro Plus software. At least five SEM images were measured for each sample to obtain accurate results.

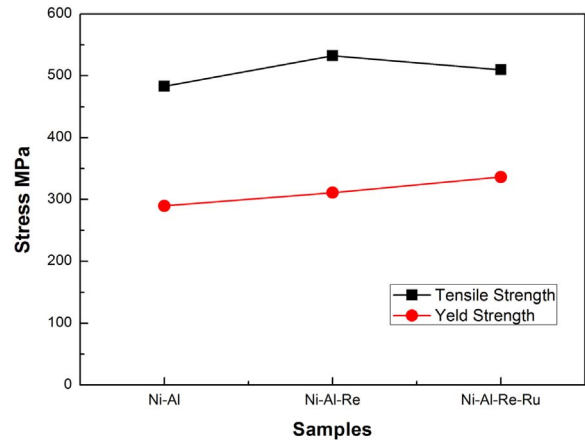


**Fig. 3.** The strength of Ni-Al, Ni-Al-Re and Ni-Al-Re-Ru model superalloys.

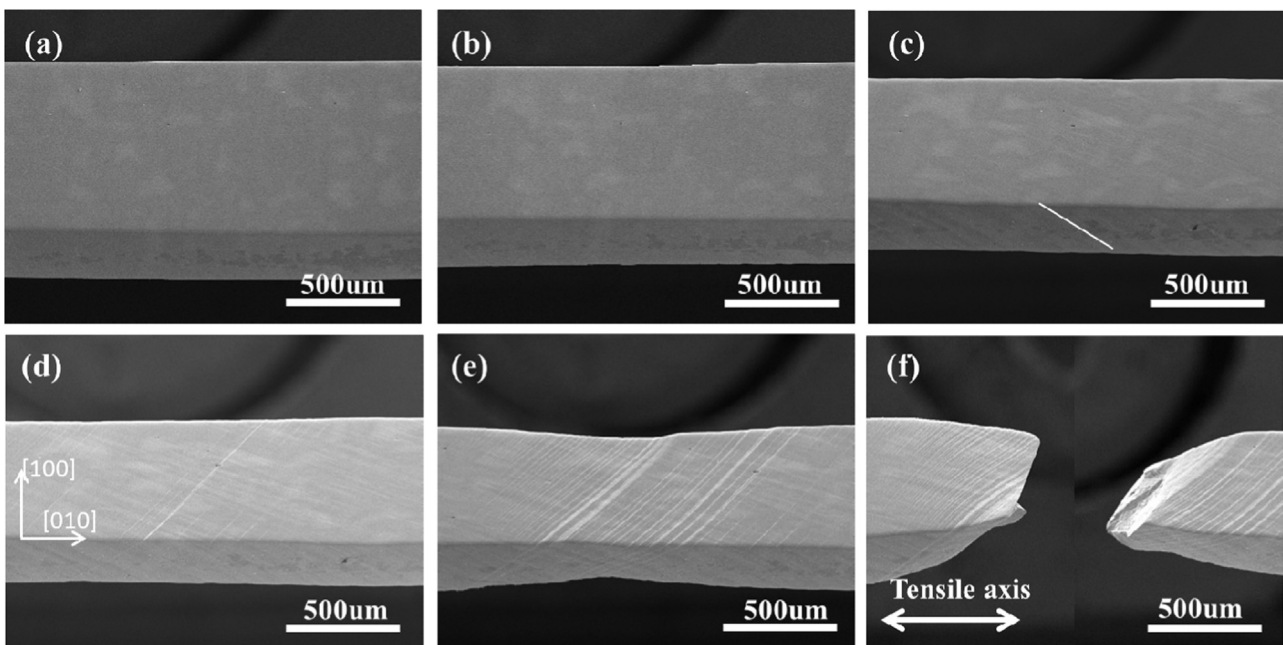


**Fig. 2.** *In-situ* tensile experiment process and fracture surface of the Ni-Al-Re model superalloy. (a) the initial state of the alloy. (b) the elastic stage of the alloy. (c) the appearance of first slip lines and the white line is the schematic slip line (d) second slip lines are activated. (e) necking propagation is induced by stress concentration. (f) fracture of alloy.

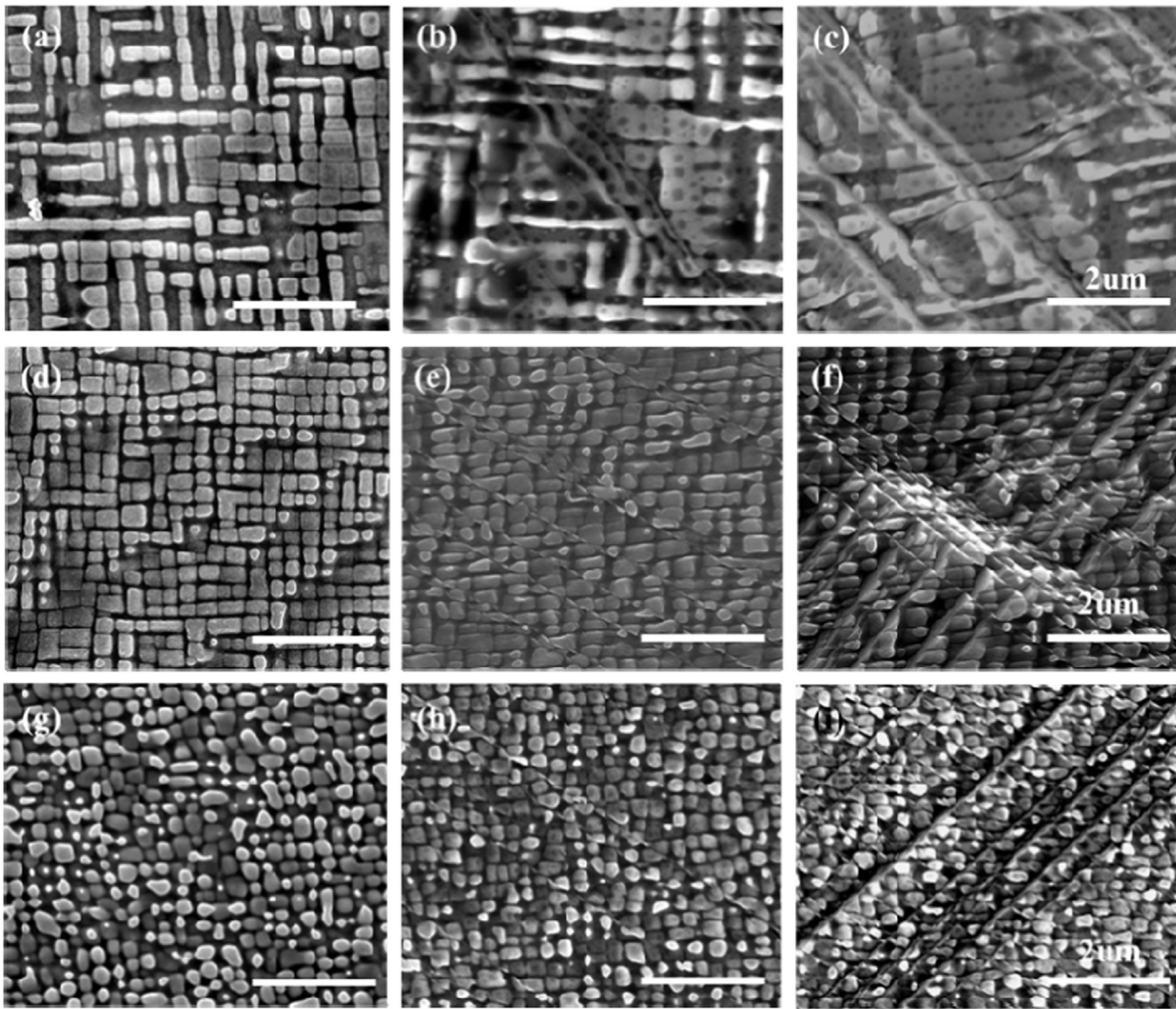


**Fig. 4.** Initial crack formation processes of the three superalloys. (a) the initial state of Ni-Al model superalloy. (b) the first slip lines are activated of Ni-Al model superalloy. (c) the second slip lines are activated of the Ni-Al model superalloy. (d, e, f) the initial state, first slip lines and second slip lines of the Ni-Al-Re model superalloy, respectively. (g, h, i) the initial state, first slip lines and second slip lines of Ni-Al-Re-Ru model superalloy, respectively.

### 3. Results

#### 3.1. *In-situ* tensile experiments

The results from the *in situ* tensile experiments of the Ni-Al-Re model superalloy are illustrated in Figs. 2a to 2f. The surface of the sample before tensile experiment is smooth without a scratch (Fig. 2a). The sample elongates homogeneously when the loading commenced, exhibiting elastic behavior, as shown in Fig. 2b. As the tensile stress increasing, the first slip lines appear with faint contrast, as depicted in Fig. 2c. To clearly show the first slip lines, a white schematic slip line is shown in sample. The sample still homogeneously elongated at this time. With the tensile stress increasing, a second set of slip lines appear interacting with the first slip lines, as shown in Fig. 2d. The deformation of the model superalloy becomes inhomogeneous and necking propagation is induced by the stress concentrated, as shown in Fig. 2e. The slip bands become wider and the slip lines grow longer. Finally, the necking propagation leads to fracture of the sample, as depicted in Fig. 2f. The *in-situ* tensile experiments of the Ni-Al and Ni-Al-Re-Ru model superalloys display similar results to those for the Ni-Al-Re

model superalloy depicted. The plastic deformation mechanism of all the three model single crystal superalloys is double-oriented slipping of dislocation. The Schmid Factor is calculated to be 0.408 and comparing the slip lines in the sample (001) plane, which is inclined to the stress axis at an angle of 45 degrees, the activated slip systems are confirmed to be (1-1-1) [01-1] and (1-11) [0-1-1].

The strength of Ni-Al, Ni-Al-Re and Ni-Al-Re-Ru model superalloys is given in Fig. 3. The yield strength for Ni-Al, Ni-Al-Re and Ni-Al-Re-Ru model superalloys is 290 MPa, 311 MPa, 336 MPa, respectively. The ultimate tensile strength for Ni-Al, Ni-Al-Re and Ni-Al-Re-Ru model superalloys is 483 MPa, 532 MPa, 510 MPa, respectively. It is concluded that Re and Ru could improve the mechanical property. The yield strength for Ni-Al, Ni-Al-Re and Ni-Al-Re-Ru model superalloys increased in sequence. The ultimate tensile strength for Ni-Al-Re is highest among them.

The microstructural evolutions of the Ni-Al, Ni-Al-Re and Ni-Al-Re-Ru model single crystal superalloys during the tensile process are shown in Fig. 4. The initial microstructure of three model superalloys is displayed in Figs. 4a, 4d, and 4g. The  $\gamma'$  precipitates are cubic in the Ni-Al and Ni-Al-Re model superalloys. In contrast, the  $\gamma'$  precipitates have



a spherical tendency in the Ni-Al-Re-Ru model superalloy. The average size of  $\gamma'$  precipitates in the Ni-Al, Ni-Al-Re and Ni-Al-Re-Ru model superalloys is 0.30  $\mu\text{m}$ , 0.24  $\mu\text{m}$ , and 0.22  $\mu\text{m}$ , respectively. The microstructure of the early plastic stages of the superalloy is exhibited in Figs. 4b, 4e, and 4h. Paralleled slip lines are observed in the three model superalloys. Both  $\gamma$  matrix and the  $\gamma'$  precipitates are subjected to severe deformation inside the slip bands. However, the  $\gamma'$  precipitates still retain their cubic shape outside of the slip bands. The microstructure of the three model single crystal superalloys during the later plastic deformation stage is shown in Figs. 4c, 4f, and 4i, in which the second set of slip lines are activated. The  $\gamma'$  precipitates and  $\gamma$  matrix are subjected to severe deformation in the slip lines. Moreover, the most acute deformation occurs at the intersection of the two sets of slip lines.

It is thought that the intersection of the two sets of slip lines will be the initiator of the micro-cracks and the experimental results support this point. A micro-crack is observed in Ni-Al model superalloy (Fig. 5), which is formed at the intersection of two sets of slip lines, resulting from the most severe plastic deformation. Stress concentration occurs at the micro-crack tips labeled as A and B and crack propagation may begin from this location.

Fig. 6a–c show the fracture surfaces of the Ni-Al, Ni-Al-Re, and Ni-

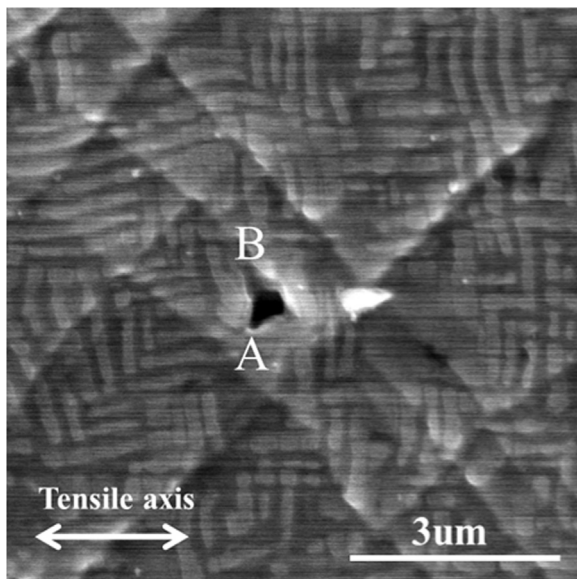


Fig. 5. Initiator of the micro-crack forms at the intersection of two sets of slip lines in the Ni-Al model superalloy.

Al-Re-Ru model superalloys, respectively. The fracture surfaces of the Ni-Al and Ni-Al-Re-Ru model superalloys are nearly parallel to (010) planes, which are perpendicular to the tensile axis, as shown in Figs. 6a and 6c. The fracture surface of the Ni-Al-Re model superalloy is along the slip plane (Fig. 6b), therefore the fracture surface is nearly parallel to the (1–11) plane. The insets in Fig. 6 are schematics of superalloys with different fracture surfaces.

### 3.2. Dislocation configurations of three model superalloys

Fig. 7 is the two beam bright field images of the Ni-Al model superalloy close to the [001] zone axis. It can be seen from Fig. 7a that there are many dislocations within the  $\gamma$  matrix and at the  $\gamma/\gamma'$  interfaces. The dislocation line '123' is cross-slip due to the dislocation line '12' and '23' is the right angle, which is in the  $\gamma$  matrix. A dimensional schematic of dislocations cross-slip in the different {111} planes of the  $\gamma$  matrix and its projection onto (001) plane are shown in the Fig. 7c. By the standard  $\mathbf{g} \cdot \mathbf{b} = 0$  invisibility criterion, the Burgers vector of dislocation in the  $\gamma'$  phase is identified as  $a[10\bar{1}]$ , which is the  $a/2 < 110 >$  partial dislocation pairs coupled with antiphase boundary (APB) as in prior reports [16,17]. A dimensional schematic of dislocation pairs coupled with APB cutting into the  $\gamma'$  phases and its projection onto (001) plane are shown in the Fig. 7d. It is thereby demonstrated that the deformation mechanism of the Ni-Al model superalloy is controlled by dislocations gliding in the  $\gamma$  matrix and dislocation pairs coupled with APB cutting into the  $\gamma'$  phases.

The dislocation configuration of the Ni-Al-Re model superalloy is shown in Fig. 8, which is the two beam bright field images close to the [001] zone axis. Many dislocations are present in the  $\gamma$  matrix and at the  $\gamma/\gamma'$  interfaces from Figs. 8a and 8b. However, the configuration of the dislocation cutting the  $\gamma'$  phases in the Ni-Al-Re model superalloy is different with that of the Ni-Al model superalloy. In addition to  $a/2 < 110 >$  partial dislocation pairs coupled with APB (Fig. 8a), there are many dislocations with stacking faults cutting the  $\gamma'$  phases [18]. By means of the partial dislocation invisible criterion  $\mathbf{g} \cdot \mathbf{b} = 0$ , or  $\pm 1/3$ , the Burgers vector of leading partial dislocation cutting into  $\gamma'$  phases is identified as  $a/3 [1\bar{1}2]$ . A dimensional schematic of dislocation pairs coupled with APB and stacking faults cutting into  $\gamma'$  phase and their projections onto (001) plane are shown in the Figs. 8c and 8d. It is therefore shown that the deformation mechanism of Ni-Al-Re model superalloy is controlled by the dislocations gliding in the  $\gamma$  matrix, dislocation pairs coupled with APB, and dislocations with stacking fault cutting into the  $\gamma'$  phases.

Fig. 9 shows the two beam bright field images of the Ni-Al-Re-Ru superalloy close to the [001] zone axis. Many dislocations are observed in the  $\gamma$  matrix and at the  $\gamma/\gamma'$  interfaces. The dislocations cross-slip is

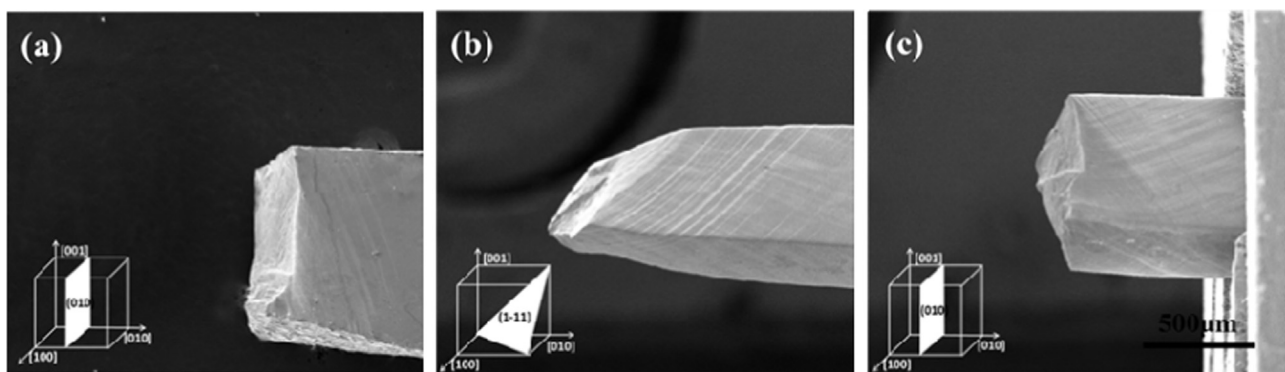
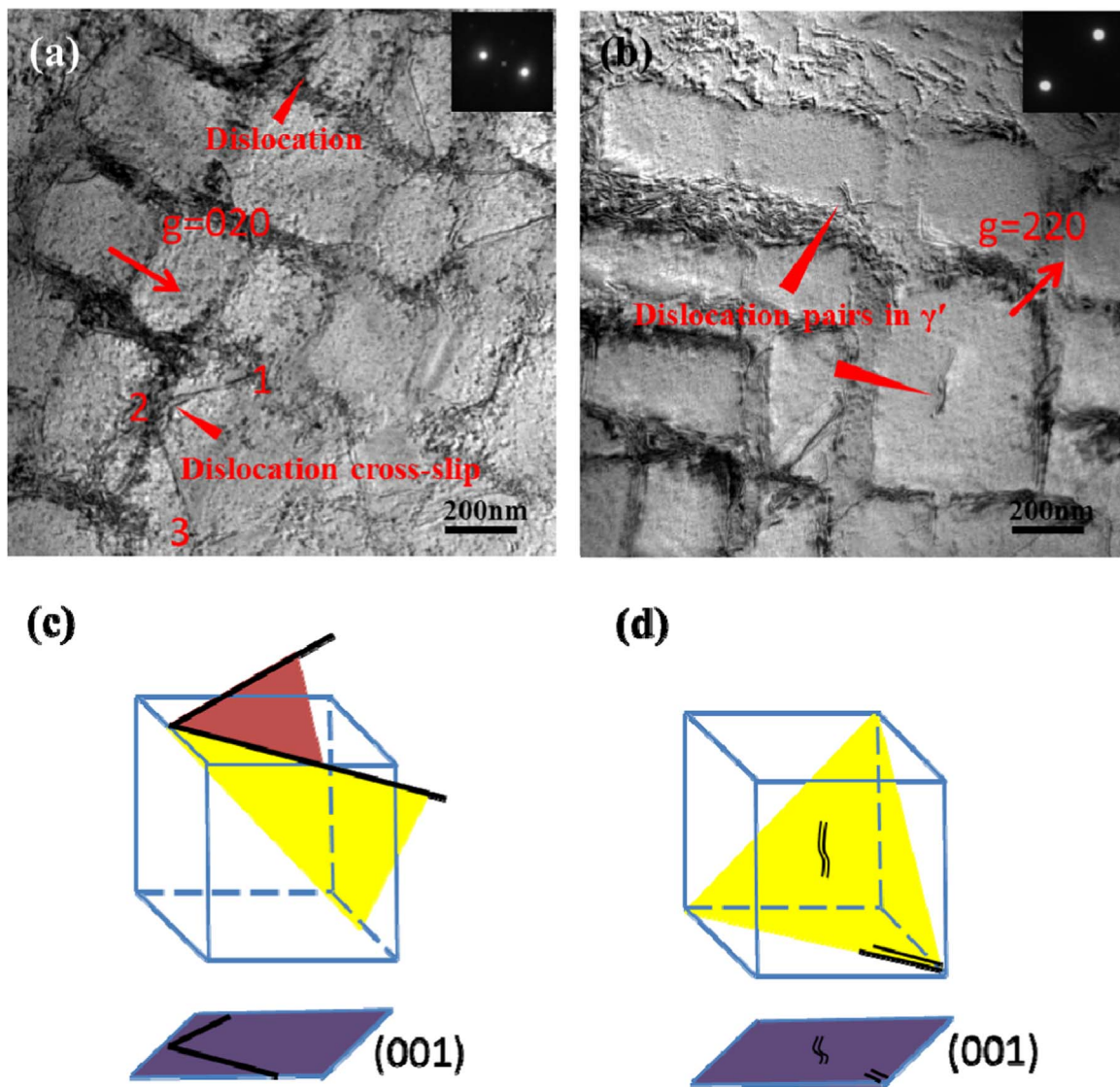


Fig. 6. Fracture surfaces of the three superalloys. (a), (b), and (c) are the Ni-Al, Ni-Al-Re and Ni-Al-Re-Ru model superalloys, respectively. The insets are schematics of the superalloys fracture surfaces.



**Fig. 7.** Dislocation configurations in the Ni-Al model superalloy. (a) Dislocations in the  $\gamma$  matrix and at the  $\gamma/\gamma'$  interfaces. (b) Dislocation pairs in the  $\gamma'$  phases. (c) Dimensional schematic of dislocations cross-slip in the different  $\{111\}$  plane of the  $\gamma$  matrix and its projection onto (001) plane. (d) Dimensional schematic of dislocation pairs coupled with APB cutting into the  $\gamma'$  phases and its projection onto (001) plane. The insets are selected area diffraction patterns (SADP), for (a),  $g=[020]$ , and (b)  $g=[220]$ . The zone axis is  $[001]$ .

also observed in the  $\gamma$  matrix of the Ni-Al-Re-Ru superalloy, as shown in Fig. 9a. The dimensional schematic of dislocations cross-slip in the different  $\{111\}$  planes of  $\gamma$  matrix and its projection onto (001) plane is shown in the Fig. 9c. In addition, some dislocation pairs coupled with APB cutting into the  $\gamma'$  phases are also observed in this superalloy, as shown in Fig. 9b. The dimensional schematic of dislocation pairs coupled with APB cutting into  $\gamma'$  phase and its projection onto (001) plane is shown in the Fig. 9d. However, the dislocations with stacking fault are not observed in case of the Ni-Al-Re-Ru superalloy. It is thereby indicated that the deformation mechanism of the Ni-Al-Re-Ru superalloy is similar to that of the Ni-Al model superalloy.

#### 4. Discussion

The results described in the previous sections detailed the effect of Re and Ru on the deformation and fracture mechanisms in nickel-based model single crystal superalloys during the *in-situ* tensile process.

The plastic deformation mechanism of all three types of model single crystal superalloys is double-oriented slipping of dislocations, as

shown in Fig. 2. The activated slip systems are considered to be (1-1-1)  $[01-1]$  and (1-1-1)  $[0-1-1]$  during the *in-situ* tensile process.

During the plastic deformation of the three superalloys, there are two ways for the dislocations cutting into the  $\gamma'$  phases, as shown in Fig. 10. The first is dislocation pairs coupled with the APB cutting into the  $\gamma'$  phases, which is common to all three superalloys (in Fig. 10a). The second is dislocations with the stacking faults cutting into the  $\gamma'$  phases, which is only observed in the Ni-Al-Re superalloy (in Fig. 10b).

It is concluded that the fracture surfaces of the model superalloys are affected by Re and Ru. Further study shows the dislocation configurations of three model superalloys also influenced by these elements. We believe that the stacking fault energy variation could explain the relationship between the crack propagation modes and the deformation mechanisms. During the tensile deformation, as the stacking fault energy is relative high for Ni-Al model superalloy [19], the dislocations could move through several slip planes by cross-slip in the  $\gamma$  channel of Ni-Al model superalloy. The  $\gamma/\gamma'$  interfaces could play a leading role in inhibiting the dislocation cutting into  $\gamma'$  phase [20]. Many dislocations are impeded at the  $\gamma/\gamma'$  interfaces. Therefore, the cracks in the Ni-Al model superalloy could easy propagate along the

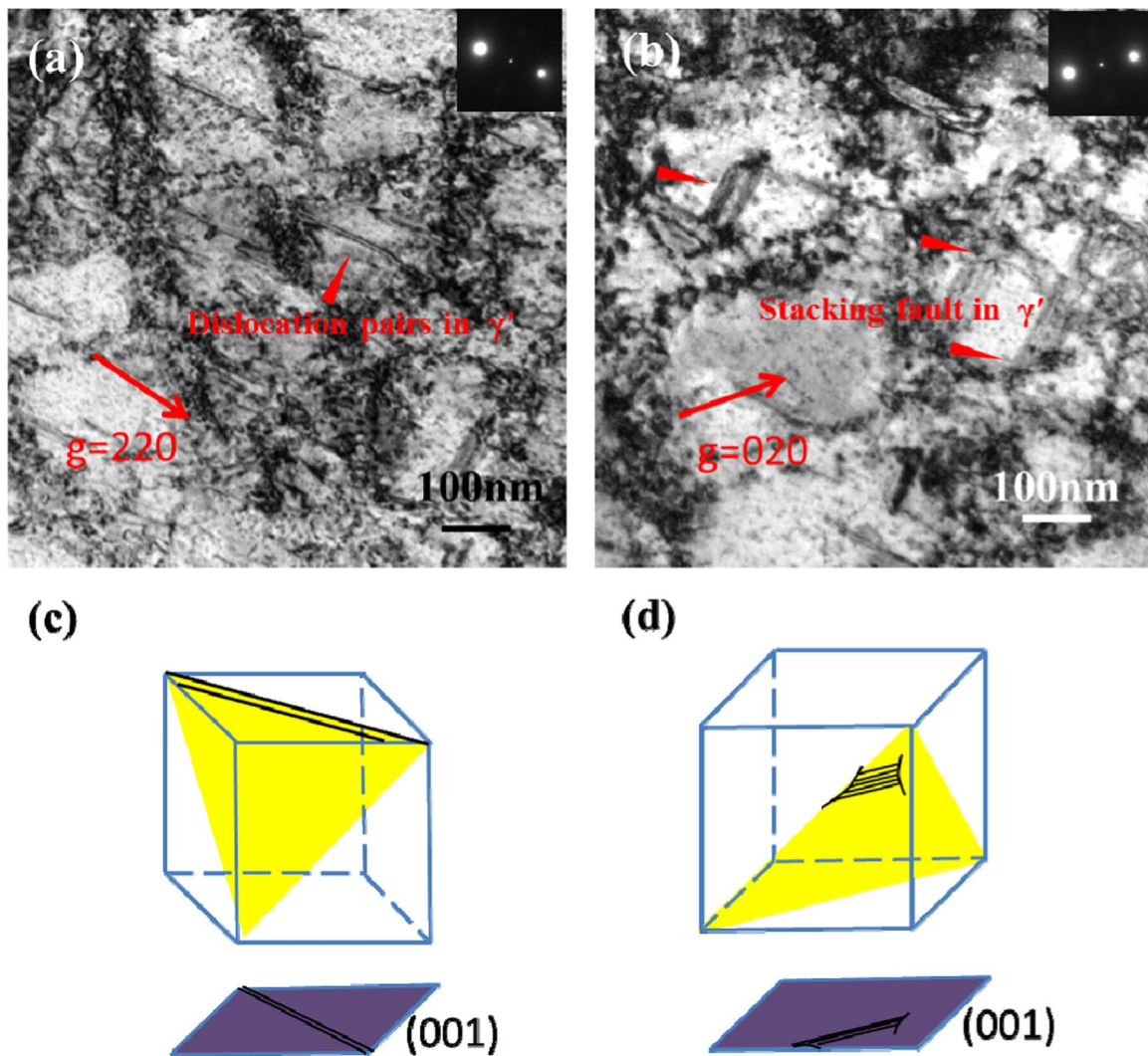


**Fig. 8.** Dislocation configurations in the Ni-Al-Re model superalloy. (a) Dislocations in the  $\gamma$  matrix and dislocation pairs coupled with the APB cutting into the  $\gamma'$  phases. (b) Dislocation pairs with stacking faults cutting into the  $\gamma'$  phases. (c) Dimensional schematic of dislocation pairs coupled with the APB cutting into the  $\gamma'$  phases and its projection onto the (001) plane. (d) Dimensional schematic of dislocation with the stacking faults cutting into the  $\gamma'$  phases and its projection onto the (001) plane. The insets are selected area diffraction patterns (SADP), for (a)  $g=[220]$  and (b)  $g=[020]$ . The zone axis is [001].

(010) cubic plane. In the Ni-Al-Re model superalloy, numerous dislocations at the  $\gamma/\gamma'$  interfaces are extended and then  $a/3[112]$  partial dislocation cut into  $\gamma'$  phase to generate the stacking fault. It is attributed to the reduction of the stacking fault energy in Ni-Al-Re model superalloy. Stacking faults generated on the  $\{111\}$  planes could inhibit other dislocations cross-slip (dislocation cross-slip is not observed in the Ni-Al-Re-Ru model superalloy), and force dislocations to slip along the single  $\{111\}$  plane. As the close-packed planes, the  $\{111\}$  slip plane has the maximum interplanar spacing and minimum binding force. Therefore, the cracks of Ni-Al-Re model superalloy propagate along  $\{111\}$  octahedral slip planes. Stacking faults are not observed in Ni-Al-Re-Ru model superalloy and it is speculated that the stacking fault energy in the Ni-Al-Re-Ru is higher than Ni-Al-Re model superalloy. The dislocation configuration is similar to the Ni-Al model superalloy. The cracks in the Ni-Al-Re-Ru model superalloy therefore propagate along the (010) cubic plane.

## 5. Conclusion

The effect of Re and Ru on the deformation and fracture mechanisms in Ni-based model single crystal superalloys was investigated. The conclusions are summarized as follows:

1. The plastic deformation mechanism of the Ni-Al, Ni-Al-Re and Ni-Al-Re-Ru model single crystal superalloys is the double-oriented slipping of dislocation at room temperature during *in-situ* tensile process. The activated slip systems are  $(1-1-1)[01-1]$  and  $(1-11)[0-1-1]$ .
2. During the tensile experiment, the initial crack often forms at the intersection of the two sets of slip lines. The cracks in the Ni-Al and Ni-Al-Re-Ru model superalloys propagate along (010) planes, and the cracks in the Ni-Al-Re model superalloy propagate along the  $(1-11)$  octahedral slip planes.
3. High density dislocations are present in the  $\gamma$  matrix and at the  $\gamma/\gamma'$  interfaces of all three superalloys. The dislocations cross-slip in the  $\gamma$  matrix and  $a/2 < 110 >$  dislocation pairs coupled with the APB are observed cutting into  $\gamma'$  phase in the Ni-Al and Ni-Al-Re-Ru superalloys. In addition to the  $a/2 < 110 >$  dislocation pairs coupled with the APB,  $a/3 < 112 >$  dislocations with stacking fault also cut into  $\gamma'$  phase in Ni-Al-Re superalloy. This is because that Re could reduce the stacking fault energy in Ni-Al-Re model superalloy. Conversely, the presence of Ru could increase stacking fault energy in Ni-Al-Re-Ru model superalloy. The different dislocations configuration may be relative to the cracks of three superalloys propagation modes.



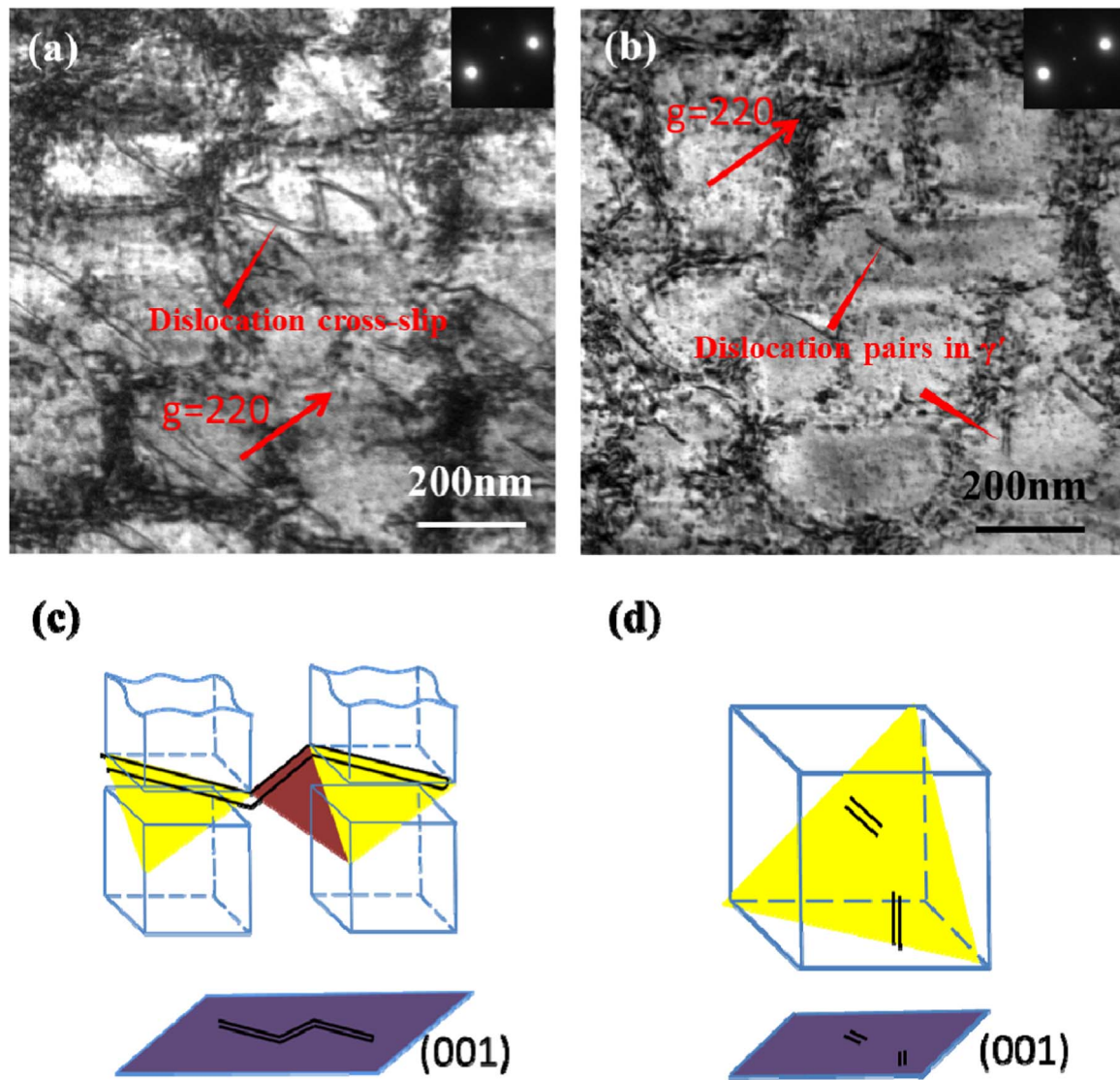


**Fig. 9.** Dislocation configurations in the Ni-Al-Re-Ru model superalloy. (a) Dislocations in the  $\gamma$  matrix. (b) Dislocation pairs coupled with the APB cutting into the  $\gamma'$  phases. (c) Dimensional schematic of dislocations cross-slip in the different  $\{111\}$  planes of the  $\gamma$  matrix and its projection onto the (001) plane. (d) Dimensional schematic of dislocation pairs coupled with the APB cutting into  $\gamma'$  phases and its projection onto the (001) plane. The insets are selected area diffraction patterns (SADP), for  $g = [220]$ . The zone axis is  $[001]$ .

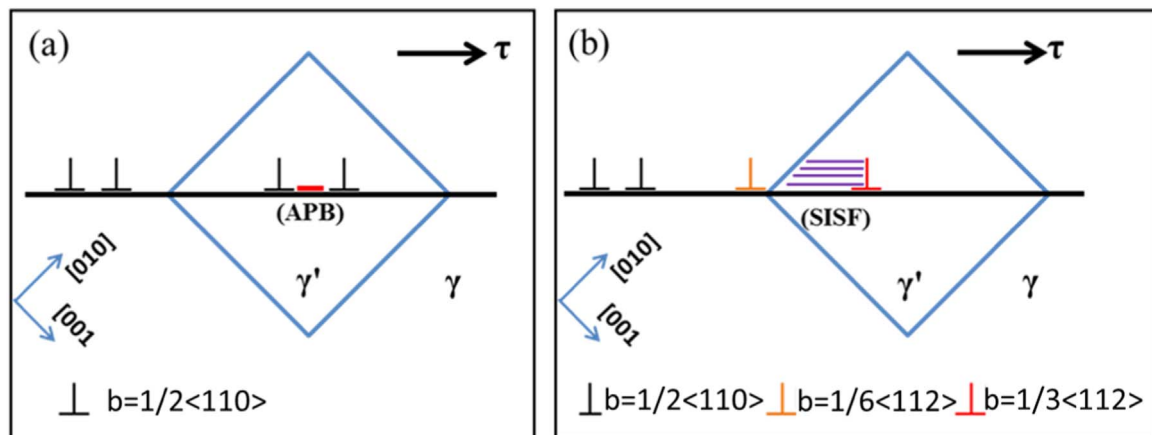


**Fig. 10.** Two ways for the dislocations to cut into the  $\gamma'$  phases. (a) dislocation pairs coupled with the APB, and (b) dislocations with the stacking faults.

## Acknowledgment

This work is supported by the National Natural Science Foundation of China (Grant Nos. 11404015 and 11327901).

## References

- [1] R.C. Reed, *The Superalloys Fundamentals and Applications*, Cambridge University Press, New York, 2006.
- [2] T.M. Pollock, S. Tin, Nickel-based superalloys for advanced turbine engines: chemistry, microstructure and properties, *J. Propul. Power* 22 (2006) 361–374.
- [3] F. Diologent, P. Caron, On the creep behavior at 1033K of new generation single-crystal superalloys, *Mater. Sci. Eng. A* 385 (2004) 245–257.
- [4] S.G. Tian, Z. Zeng, C. Zhang, C. Liu, Creep behavior of a 4.5%-Re single crystal nickel-based superalloy at intermediate temperatures, *Mater. Sci. Eng. A* 543 (2012) 104–109.
- [5] W.Z. Wang, T. Jin, J.L. Liu, X.F. Sun, Role of Re and Co on microstructures and  $\gamma'$  coarsening in single crystal superalloys, *Mater. Sci. Eng. A* 479 (2008) 148–156.
- [6] C.M.F. Rae, R.C. Reed, The precipitation of topologically close-packed phases in rhenium-containing superalloys, *Acta Mater.* 49 (2001) 4113–4125.
- [7] K. Cheng, T. Jin, Z. Hu, Effect of Re on the precipitation behavior of  $\mu$  phase in several single crystal superalloys, *J. Alloy. Compd.* 536 (2012) 7–19.
- [8] A. Sato, H. Harada, T. Yokokawa, T. Murakumo, Y. Koizumi, T. Kobayashi, H. Imai, The effects of ruthenium on the phase stability of fourth generation Ni-base single crystal superalloys, *Scr. Mater.* 54 (2006) 1679–1684.
- [9] L.J. Rowland, Q. Feng, T.M. Pollock, Microstructural stability and creep of ru-containing nickel-base superalloys, *Ann. Arbor., Superalloys* (2004) 697–706.
- [10] L.J. Carroll, Q. Feng, J.F. Mansfield, T.M. Pollock, Elemental partitioning in Ru-containing nickel-base single crystal superalloys, *Mater. Sci. Eng. A* 457 (2007) 292–299.
- [11] X.P. Tan, J.L. Liu, T. Jin, Z.Q. Hu, H.U. Hong, B.G. Choi, I.S. Kim, C.Y. Jo, D. Mangelinck, Effect of Ru additions on very high temperature creep properties of a single crystal Ni-based superalloy, *Mater. Sci. Eng. A* 580 (2013) 21–35.
- [12] S.G. Tian, X. Ding, Z. Guo, J. Xie, Y. Xue, D. Shu, Damage and fracture mechanism of a nickel-based single crystal superalloy during creep at moderate temperature, *Mater. Sci. Eng. A* 594 (2014) 7–16.
- [13] J.J. Moverare, S. Johansson, R.C. Reed, Deformation and damage mechanisms during thermal–mechanical fatigue of a single-crystal superalloy, *Acta Mater.* 57 (2009) 2266–2276.
- [14] M. Ott, H. Mughrabi, Dependence of the high-temperature low-cycle fatigue behaviour of the monocrystalline nickel-base superalloys CMSX-4 and CMSX-6 on the  $\gamma/\gamma'$  morphology, *Mater. Sci. Eng. A* 272 (1999) 24–30.
- [15] Q. Shi, X. Ding, J. Chen, X.N. Zhang, Q. Feng, Fracture mode of a Ni-based single crystal superalloy containing topologically close-packed phases at ambient temperature, *Metall. Mater. Trans. A* 45 (2014) 1665–1669.
- [16] J.X. Zhang, T. Murakumo, Y. Koizumi, T. Kobayashi, H. Harada, Slip geometry of dislocations related to cutting of the  $\gamma'$  phase in a new generation single-crystal superalloy, *Acta Mater.* 51 (17) (2003) 5073–5081.
- [17] C.Y. Chen, R. Schaublin, W.M. Stobbs, Investigation of interfacial segregation at antiphase boundaries in a ternary alloy 84.8 Ni–12.8 Al–2.4 Ta, *Mater. Sci. Eng. A* 360 (2003) 356–364.
- [18] D.M. Knowles, Q.Z. Chen, Superlattice stacking fault formation and twinning during creep in  $\gamma/\gamma'$  single crystal superalloy CMSX-4, *Mater. Sci. Eng. A* 340 (2003) 88–102.
- [19] N.C. Eurich, P.D. Bristowe, Segregation of alloying elements to intrinsic and extrinsic stacking faults in  $\gamma'$ -Ni3Al via first principles calculations, *Scr. Mater.* 102 (2015) 87–90.
- [20] M. Huang, Z. Cheng, J. Xiong, J. Zhu, Coupling between Re segregation and  $\gamma/\gamma'$  interfacial dislocations during high-temperature, low-stress creep of a nickel-based single-crystal superalloy, *Acta Mater.* 76 (2014) 294–305.